Batista-Grau, P.; Fernández Domene, RM.; Sánchez-Tovar, R.; Blasco-Tamarit, E.; Solsona, B.; Garcia-Anton, J. (2022). Indirect charge transfer of holes via surface states in ZnO nanowires for photoelectrocatalytic applications. Ceramics International. 48(15):21856-21867. https://doi.org/10.1016/j.ceramint.2022.04.170

Indirect charge transfer of holes via surface states in ZnO nanowires for photoelectrocatalytic applications

P. Batista-Grau [a], R.M. Fernández-Domene [b], R. Sánchez-Tovar [b], E. Blasco-Tamarit[a], B. Solsona[b] J. García-Antón [a]*.

[a] *Ingeniería Electroquímica y Corrosión (IEC), Instituto Universitario de Seguridad Industrial, Radiofísica y Medioambiental (ISIRYM), Universitat Politècnica de València, Camino de Vera s/n, 46022 Valencia, Spain.* * *jgarciaa@iqn.upv.es*

[b] *Departamento de Ingeniería Química, Universitat de València, Av de les Universitats, s/n, 46100 Burjassot, Spain.*

Abstract

In this work, ZnO nanowires with high aspect ratio were obtained by fast and simple electrochemical anodization. Morphological, structural and photoelectrochemical characteristics of the synthesized ZnO nanowires were evaluated by using different techniques: field emission scanning electron microscopy, atomic force microscopy, high resolution transmission electron microscopy, Raman spectroscopy, X-ray diffraction, X-ray photoelectron spectroscopy, UV–VIS spectroscopy, Mott-Schottky analysis and photoelectrochemical impedance spectroscopy. The synthesized ZnO nanowires presented high roughness and high crystallinity. Besides, surface defects were identified in the sample. The value of the donor density (N_D) was in the order of 10^{19} cm^{-3} in the dark and 10^{20} cm^{-3} under illumination. In addition, the ZnO nanowires presented good photosensibility, with a photocurrent density response 85 times higher than a ZnO compact layer, and lower resistance to charge transfer. The charge transfer processes taking place at the ZnO/electrolyte interface were studied, since these processes strongly influence the photoelectrocatalytic efficiency of the material. According to the results, the charge transfer of holes in the synthesized ZnO nanowires occurs indirectly via surface states. In this regard, surface states may be an important feature for photoelectrocatalytic applications since they could provide lower onset voltages and higher anodic current densities.

Keywords: ZnO nanowires, charge transfer, surface states, XPS, photoelectrochemical impedance spectroscopy.

1. Introduction

Problems associated with the use of fossils fuels as primary energy source promote the development of clean and sustainable energy systems [1]. In this context, the energy from the Sun is the most abundant energy source [2,3]. In contrast to most energy sources, it is completely clean and free [4]. Nevertheless, its intermittency due to diurnal and stational variations [5] and the permanent energy demand [2,6] constitutes the main challenges concerning its broad use. A promising solution is the storage of the solar energy by its direct conversion into chemical fuels, such as hydrogen, by using semiconductor materials for light harvesting [7–9].

Since titanium dioxide (TiO_2) was employed by Fujishima and Honda in the 70s as a photoanode of a water splitting photoelectrochemical cell [10], TiO_2 has been the most studied material for this application [11]. However, interest in other materials such as zinc oxide (ZnO) has increased in the last few years. ZnO is an n-type semiconductor with a wide direct band gap value (~3.3 eV), very similar to TiO_2, that mainly allows light absorption in the UV range. It presents high charge carriers mobility of 200 $cm^{-2}V^{-1}s^{-1}$ for the electrons and 180 $cm^{-2}V^{-1}s^{-1}$ for the holes [12] and a higher electron diffusivity than TiO_2 [13]. In addition, it is nontoxic [14–16], biologically compatible [17] and biodegradable [14], facile to synthesize [18], non-expensive [11,19] and presents high photostability [7]. Hence, ZnO is an interesting material that could be used to replace TiO_2 in photocatalytic and photoelectrocatalytic applications. It could be employed, for example, to split the water molecule upon irradiating the semiconductor electrode in an electrolyte with the aim of obtaining hydrogen or to generate hydroxyl radicals from water oxidation which, in turn, could oxidize organic pollutants present in wastewaters. In that sense, Hernandez et al. [11] observed a better photoelectrochemical behavior of ZnO nanowires compared to different TiO_2 nanostructures.

Nanostructuring strategies have been employed in order to enhance photoelectrocatalytic performance of materials [9]. Since nanostructured morphology increases the specific surface area, light absorption is enhanced [20] and thus, more carriers are photogenerated [21]. Moreover, the electron and holes recombination is decreased owing to the reduction of the diffusion path lengths [20]. Additionally, the type and the size of the nanostructured morphology strongly influence the photoelectrocatalytic performance of ZnO [22–24]. In particular, one-dimensional morphology, including nanowires, presents certain

advantages [25] such as a significant surface-to-volume ratio [20] that enhances light absorption and a remarkably improved charge transfer along the longitudinal direction, which promotes the separation of the photogenerated charge carriers decreasing recombination [26]. Besides, the thin walls created due to the small wire diameter enhance hole diffusion towards the electrolyte [27].

So far, several methods have been used to synthesize ZnO nanostructures. These methods can be divided into vapor-phase-based methods and liquid-phase-based methods. Examples of vapor-phase-based methods are sputtering, thermal evaporation or pulsed laser deposition. Concerning liquid-phase-based methods, techniques such as sol-gel, hydrothermal or electrochemical methods fall within this second type [28]. Among these liquid-phase methods, electrochemical anodization seems to be very promising since it is relatively low cost, simple, and fast [20]. In addition, it allows large-scale synthesis [20] and a great controllability in size and morphology of the synthesized nanostructures. All these facts contrast with the majority of methods that require complicated procedures [29], costly setups [29,30] and specific environmental conditions [22], or long reaction times [29,30]. Moreover, through anodization the nanostructures grow directly on the metallic zinc substrate, acting as the back contact of the photoanode [20,25,31]. Among the electrolytes employed for the anodization of zinc, bicarbonate-based solutions seem to be very interesting since they allow the ZnO nanowires formation at room temperature, low voltages (10 V) and short times (10 min), as reported in previous works [20,24].

A simple photoelectrochemical (PEC) cell configuration for water splitting using an n-type semiconductor consists of a photoanode and a metal cathode, both immersed in an electrolyte [32]. When the photoanode is under illumination, it absorbs photons with energy higher than the band gap energy of the semiconductor and, consequently, electrons from the valence band are excited to the conduction band, producing a positive hole in the valence band. These photogenerated electrons and holes are spatially separated since an electric field is formed inside the semiconductor, thereby preventing recombination. Nevertheless, an external bias is applied in order to enhance charge separation and kinetics. The photogenerated electrons are aimed at the metallic back contact and are transported via an external wire to the metallic cathode where they reduce water with the subsequent formation of hydrogen gas. The photogenerated holes are driven to the semiconductor/electrolyte interface, where water oxidation takes place [12].

Apart from the production of hydrogen through photoelectrochemical water splitting, ZnO nanostructures can also be used in other photoelectrocatalytic applications, such as in dye sensitize solar cells (DSSCs) to produce electricity from solar light and in the degradation of persistent and toxic organic compounds from wastewaters via the generation of hydroxyl radicals by electron holes [28].

Photoelectrocatalytic efficiency of semiconductors is dependent on charge transfer and recombination competition and on charge trapping events which take place at the semiconductor/electrolyte interface under illumination [8]. Therefore, knowledge of these interfacial characteristics is essential to achieve an enhancement of the semiconductors performance for its application in solar fuel production [7,33]. Two types of charge transfer mechanisms have been described in scientific publications: hole transfer directly from the valence band and indirectly via surface states [7]. Surface states are modifications that occur on the surface with respect to the bulk of the semiconductor. These states appear as a consequence of the sudden termination of the crystal lattice and can be caused by the adsorption of electrolyte molecules, vacancies and other structural defects that occur on the surface [32,34]. These states could introduce energetic levels between the semiconductor valence band and the conduction band [34,35], that could act as recombination centers or, on the contrary, may enhance charge transfer [36]. In the latter, surface states could be an important feature for hydrogen production since they could facilitate lowering onset voltages and higher anodic photocurrent densities [7,37]. In this context, photoelectrochemical impedance spectroscopy (PEIS) is a powerful technique for the study of recombination and charge transfer processes occurring at the semiconductor/electrolyte interface under illumination [34].

The major aim of this work is to investigate the charge transfer mechanism under simulated solar light of ZnO nanowires synthesized by simple anodization in bicarbonate electrolyte. The knowledge of the charge transfer mechanism is important to subsequently design and fabricate tuned nanostructures in order to enhance their photoelectrocatalytic performance. Additionally, the knowledge of the morphological and structural characteristics of the nanostructures is evaluated through field emission scanning electron microscopy, atomic force microscopy, high resolution transmission electron microscopy, Raman spectroscopy, X-ray diffraction, X-ray photoelectron spectroscopy and UV–VIS spectroscopy. Likewise, the photoelectrochemical behavior of the samples is examined.

Finally, the samples are studied by Mott-Schottky analysis and photoelectrochemical impedance spectroscopy (PEIS).

2. Experimental procedure

2.1. Synthesis

On the one hand, ZnO nanowires were formed by electrochemical anodization in a 2-electrode cell with a zinc rod (99,999 % purity, 8mm) anode and a platinum foil cathode (Figure S1). On the other hand, a ZnO compact layer was fabricated for comparison by etching the zinc rod in a solution of 5 % HCl for 30 s [34]. Previously to anodization, the zinc rod surface was polished with 240–4000 SiC papers to achieve a mirror finish. Next, the degreasing of the samples was carried out by sonication in ethanol for 2 min. Then, the electrodes were rinsed with distilled water, dried in an air stream and covered with Teflon to just expose the top surface (0.5 cm^2) to the electrolyte. Anodization was performed in a 50 mM $NaHCO_3$ aqueous electrolyte containing 10 v/v % ethanol at 10 V for 10 min at room temperature [24]. During the process, current density versus time was recorded. Once the ZnO nanostructures were formed on top of the Zn rods, thin slices (4-5 mm in height) were cut from these rods by using a cutting machine. Nanostructures were protected lest they undergo damage during this process. Finally, thermal annealing of the as-prepared samples was carried out at 300 ºC for 1 hour in air atmosphere.

2.2. Morphological characterization

The morphology of the electrodes was examined by using a Field Emission Scanning Electron Microscope (FE-SEM), while the nano-scale roughness of the samples was characterized by means of an Atomic Force Microscope (AFM) using AC mode with an oscillating cantilever (0.5 V). The parameter Sa (arithmetical mean height of the surface) was calculated to evaluate the surface roughness of the electrodes. Structural, compositional and morphological characterization of the nanostructures was also carried out by Transmission Electron Microscopy (TEM) and high resolution TEM (HRTEM). The equipment used is a FEI Field Emission Gun (FEG) TECNAI G2 F20 S-TWIN microscopy working at 200 kV. Energy Dispersive X-ray Spectroscopy (EDX) in TEM nanoprobe mode was used to obtain the chemical composition of the nanostructures. A piece of the samples was cut and sonicated in ethanol for several minutes. Then a drop of that mixture was deposited onto a holey carbon film supported on a copper grid. Finally, this was dried to be ready for the study.

2.3. Structural characterization

The crystallinity of the samples was analyzed by confocal laser-Raman spectroscopy using a blue laser (488 nm) and by X-ray diffraction (XRD) analysis using an D8AVANCE diffractometer (Bruker) equipped with a monochromatic Cu Kα1 source. Additionally, the chemical states of the ZnO nanowires were analyzed by means of X-ray photoelectron spectroscopy (XPS, K-ALPHA, Thermo Scientific). Al-K_ radiation (1486.6 eV) monochromatized by a twin crystal monochromator providing a focused X-ray spot at 3 mA × 12 kV was employed to collect the spectra. The alpha hemispherical analyzer operated in the constant energy mode by using 200 eV in a survey scan passing energies for the whole energy band measurements and 50 eV in a narrow scan for the elements. Avantage software was employed to analyze XPS data. The experimental backgrounds were approximated by using a smart background function and the surface elemental composition was calculated from the background-substracted peak areas. The system flood gun yielding from a single source low energy electrons and low energy argon ions provided the charge compensation. In the processing of the data from the XPS spectra, the values of the binding energy (BE) were referenced to the carbon (C 1s) peak at 284.5 eV. The samples were also characterized by UV-vis diffuse reflectance. DR-UV-Vis. spectroscopy measurements of the samples were carried out within the 200-850 nm range using a Shimadzu spectrometer model UV-1800. The spectra shown has been obtained from that of the untreated ZnO sample (ZnO over the Zn support) extracting the signal of the Zn support. The value of the band gap, *Eg*, was obtained by extrapolating the linear fitted region at $[F(R(\infty))h\upsilon]^2 = 0$ in the plot of $[F(R(\infty))\ h\upsilon]^2$ versus $h\upsilon$.

2.4. Electrochemical and photoelectrochemical characterization

For the electrochemical and photoelectrochemical characterization, different experiments were performed, such as water splitting tests, photoelectrochemical impedance spectroscopy (PEIS) measurements and Mott-Schottky (MS) analysis. All these experiments took place in a three-electrode configuration cell with a 0.24 M Na_2S and 0.35 M Na_2SO_3 aqueous solution as electrolyte. The zinc oxide samples were used as the photoanodes (with 0.26 cm^2 of exposed effective area), a platinum foil (1cm^2) as the cathode and an Ag/AgCl electrode as the reference electrode. The electrodes were immersed in the electrolyte and connected to a potentiostat (Autolab). Simulated sunlight conditions were carried out using AM 1.5 illumination (100 mW/cm^2).

Photocurrent density as a function of the applied potential was registered by chopped light radiation (60 s dark/ 20 s light) with a potential scan from −1.0 V to -0.2 V (rate of 2 mV/s) employing a potentiostat. Mott-Schottky analyses in dark and illumination conditions were carried out by sweeping the potential from -1.0 to -0.2 V, with an amplitude signal of 0.01 V at a frequency value of 5 kHz. PEIS experiments were carried out by using different applied potentials (vs. Ag/AgCl) over a frequency range from 100 kHz to 10 mHz with an amplitude of 0.01 V, in illumination conditions. The experimental data from PEIS measurements were fitted to the equivalent circuit by using Zview software. The aim of this set of tests was to investigate the influence of applied potentials on the impedance parameters, especially on the capacitance associated with the charge transfer of holes, in order to discover the mechanism involved in that charge transfer. Therefore, a wide range of potentials was selected.

3. Results and discussion

3.1. Morphological and structural characterization

3.1.1. Field Emission Scanning Electron Microscopy and Atomic Force Microscopy

Figure 1 shows the FESEM image of the top (a) and the cross-section (b) view of the annealed sample synthesized by electrochemical anodization. In order to compare the morphology of the anodized sample with that of a compact ZnO layer, the surface of the last sample (compact) is shown in Figure 1c. It can be noticed that the ZnO anodized sample shows a unidimensional morphology of flower-like nanowires. These nanowires present a high aspect ratio (i.e., a high surface/volume ratio) with an average length of 5.25 (± 0.24) μm and a very small diameter of the order of some nanometers. The length of the nanowires was measured from cross-section FESEM images by using a FESEM analysis software. A high aspect ratio provides an enhancement in photoelectrocatalytic performance since it improves the charge separation and increases the specific surface area [38]. In the cross-section view of the sample (Figure 1 (b)), two layers are observed. The inner layer is formed by thicker nanorods while the outer layer is formed by thinner nanowires. This is in agreement with the growth mechanism of the ZnO nanowires described in the literature for electrochemical anodization in bicarbonate solutions in which nanowires are formed from the enlargement of thicker nanorods [30]. These nanorods are grouped together constituting densely packed nanoflowers distributed over

the surface and grew from the same nucleation point within or near the pits that initially were formed in the metallic surface due to zinc dissolution [30,39–41]. A complete explanation of the ZnO nanorods growth mechanism (dissolution-precipitation mechanism) was given in previous works [20,28]. On the other hand, the image of the ZnO compact layer (Figure 1c) shows a homogeneous surface with very little roughness, indicating that, in fact, a compact oxide layer was formed.

To analyze the surface roughness of the ZnO electrodes, the arithmetical mean height of the surface, Sa, was calculated from AFM analysis. Sa for the ZnO nanowires is 808.37 nm, while it is 75.83 nm for the compact layer. As it was expected, this value is much higher for the ZnO nanowires sample than for the compact layer since the nanostructured form provides roughness to the electrode. In this regard, high value of roughness might be favorable to obtain higher surface areas for photoelectrocatalytic hydrogen production [42].

3.1.2. High resolution transmission electron microscopy

A High Resolution TEM study has been conducted in order to obtain a view of the ZnO structures at a nanometric scale and to get further insights into the morphological properties of the samples. This study was undertaken using pieces of the nanostructures drawn by scratching the surface of the sample holder so that the ZnO active material can be analysed.

According to the FESEM study, narrow and long nanowires with an average length of ca. 5 μm have been observed in the the ZnO anodized sample. This observation has been confirmed by the HRTEM study. Figure 2(a,b) shows the image of two individual nanowires of the ZnO anodized sample. An analysis of many pictures taken shows that the particles present a homogeneous cylindrical shape although with variable size. Thus, the width of the wires ranges from 50 to 250 nm. Moreover, it can be clearly observed that the structures are highly porous, this porosity mainly presenting an orientation perpendicular to the axis of the nanowires. According to the TEM images, these nanowires consist of a set of stacked disks of ca. 10-20 nm. Therefore, these nanostructures present an enhanced surface area due not only to the nanowire morphology but also to the inner porosity. These features suggest improved electrochemical properties and a potentially remarkable production of photoelectrocatalytic hydrogen.

Figure 2(c,d) shows the image of two individual particles of the ZnO compact layer. For this sample the homogeneity is not so evident, as two different morphologies can be observed: i) most of the particles analyzed (80%) consist of compact structures without porosity (Figure 2d), ii) a few particles are formed by the agglomeration of nanoparticles, leading to an interparticular porosity (Figure 2c).

The interplanar distances were measured on selected particles of the samples in order to determine the Zn phases formed. The only Zn-containing phase observed in both samples was ZnO wurtzite (JCPDS: 036–1451) which is in agreement with the interplanar distances determined from the diffraction rings (2.81, 2.60, 2.48, 1.62 and 1.38 Å). These values correspond to the (100), (002), (101), (110) and (112) family planes. The formation of only wurtzite is in agreement with that observed by other characterization techniques (qv post).

3.1.3. Raman spectra

The crystallinity and the vibrational characteristics of the ZnO samples were examined through Raman spectroscopy. The optical phonon modes at the irreducible Brillouin region of the ZnO wurtzite structure are shown as follows: $\Gamma = A_1 + 2\ B_1 + E_1 + 2\ E_2$ [19,22,43]. A_1 and E_1 divide into transverse and longitudinal optical phonons (TO and LO) [19,22,43,44]. The frequencies of these phonons are: A_1 (TO) = 380 cm^{-1}, E_1 (TO) = 407 cm^{-1}, A_1 (LO) = 574 cm^{-1}, E_1 (LO) = 581 cm^{-1} [22,45]. In addition, mode B_1 is silent [19,43] and E_2 exhibit two modes of low and high frequency phonons located at 101 cm^{-1} and 437 cm^{-1}, respectively [19,43]. Figure 3 presents the Raman scattering spectra of the ZnO nanowires and the compact layer. For the ZnO nanowires peaks associated with the ZnO hexagonal wurtzite structure are showed. Peak E_2 (high) is characteristic of the wurtzite phase [22,44,46] and its high intensity in relation to the other peaks reveals that the sample of ZnO nanowires presents high crystallinity [44]. A_1 (LO) and E_1 (LO) phonon modes are dependent on the oxygen stoichiometry [47] and, thus, they are commonly identified with defects in the crystalline structure, such as oxygen vacancies and zinc interstitial [22,46,48–50]. Thereby, the presence of these peaks in the sample of the ZnO nanowires unveiled the presence of some of these structural defects [47,49,50]. Additionally, peaks related to the scattering of the Raman second order were observed for the ZnO nanowires: 2 TA/2 E_2 (low) at 202 cm^{-1}, E_2 (high) - E_2(low) at 333 cm^{-1} , associated with ZnO vibration, 2 LO A_1 and E_1 at the frequencies of 1105 cm^{-1} and 1158 cm^{-1} [20]. On the other hand, the ZnO compact layer presented poor crystallinity and high

amount of structural disorders, given by the low intensity of the peak E_2 (high) and the high intensity of the A_1 (LO) and E_1 (LO) phonon modes.

3.1.4. XRD and XPS analysis

The crystal phase and the chemical states of the ZnO nanowires were studied by means of XRD and XPS analyses. Figure 4 shows the XRD pattern of the annealed sample in which both peaks from ZnO hexagonal wurtzite structure (marked with red circles) [19,25,51–56] and polycrystalline Zn substrate (marked with green triangles) [25,39,51,54,56] are noticed. The principle diffraction peak located at 36.4 degrees is characteristic of the ZnO wurtzite phase [25] and indicates the preferential orientation of the nanostructures along the (101) plane [19]. Other characteristics peaks of the ZnO wurtzite phase appear roughly at 32, 34.5, 48, 57, 63 and 68 degrees corresponding to (100), (002), (102), (110), (103) and (112) orientation, respectively [19,25,51–56]. According to the XRD results, the ZnO nanowires present good crystalline structure with high crystallinity [53], which is in concordance with the results showed in the Raman spectra.

Figure 5 shows the XPS wide survey spectra of the ZnO nanowires where Zn, O and C peaks were identified. The identified C is related to adventitious and residual carbon in the sample since anodization was carried out in an electrolyte based on bicarbonate solution containing ethanol. The intensive peaks of the binding energies associated with Zn $2p_{1/2}$, Zn $2p_{3/2}$ and O 1s corresponds to XPS core levels of matrix elements of ZnO wurtzite structure [57].

In order to explore more bonding details, Figure 6 shows the XPS spectra from the Zn 2p and O 1s core levels. On the one hand, Zn 2p core level (Figure 6 (a)) was fitted with a doublet located at about 1044.08 and 1021.08 eV, associated with the 2 $p_{1/2}$ and 2 $p_{3/2}$ [47,58–65]. The difference in the binding energy of the Zn $2p_{1/2}$ and Zn $2p_{3/2}$ is 23 eV and its intensity ratio is 1:2, which matches the standard reference of ZnO [47,64]**.** Besides, the binding energy of the Zn 2p peaks and its difference reflect that the chemical valence of the Zn at the nanowires surface is +2 oxidation state [47,62]**.** On the other hand, the deconvolution of the O 1s spectra of the ZnO nanowires (Figure 6 (b)) shows the formation of three peaks marked as O 1s (A), (B) and (C), and located at 529.84, 531.28 and 532.85 eV, respectively. This asymmetry in the O 1s curve reflects the variation of the oxygen oxidation number [47]. The most prevailing peak located at 529.84 eV is

related to O^{-2} ions in wurtzite structure of the hexagonal Zn^{+2} ion array [47,50,62,63,66]. Therefore, it can be identified with Zn–O bonds [47,63,67,68]. On the other hand, O 1s medium binding energy, O 1s (B), is mostly associated with oxygen vacancies or defects [49,50,62,66,68], related to O^{-2} ions within the ZnO matrix in the regions presenting oxygen deficiency [49,62]. In this regard, Wang [50] reported an increase in the intensity of this peak in XPS analysis when increasing the intensity of the peak associated with oxygen vacancies and defects in Raman, A_1 and E_1 (LO). Likewise, O 1s (C) peak is mostly identified with the existence of weakly bound oxygen on ZnO surface [50], in particular with chemisorbed or dissociated oxygen species [66,68] such as hydroxyl ygroups, i.e. Zn-OH and H_2O, strongly linked to surface disorders on ZnO [66]. Therefore, O1s deconvolution unveiled, firstly, the presence of the Zn–O bonds through the dominant peak, O 1s (A) and, secondly, the presence of surface structural disorders in the form of oxygen vacancies and hydroxyl groups that could introduce located surface states that could facilitate the trapping and detrapping of photogenerated electrons and holes [66].

3.1.5. DR-UV-Vis. study

The DR-UV-Vis. absorbance spectra of the differently synthesized ZnO samples are shown in Figure 7. As in both cases the samples consist of pure ZnO, the overall aspect of the spectra are similar, as an intense band from 200 to ca. 400 nm can be observed. [69]. However, notorious differences can be appreciated. Then, for the ZnO nanowires the intensity of the signal is remarkably larger (higher absorbance) than that of the ZnO compact layer. This enhanced amount of light absorbed can be linked to the ease for electron transfer and, probably, to their enhanced photochemical properties. This higher absorption for the nanowires is especially notorious in the UV range. Additionally, the 200-400 nm band shifts towards higher wavelengths in the ZnO nanowires. The displacement in the absorption maxima from ca. 300 nm in the reference ZnO to ca. 360 nm in the ZnO nanowires is in accordance with the formation of the nanostructures, in this case with nanowire shape.

The energy of the band gaps were also determined by using the Tauc formula [70, 71] The reference ZnO sample (consisting of a compact layer) presents a bandgap width of 3.18 eV, which is higher than that observed for ZnO nanowires (3.11 eV). This lower value observed for the bandgap of the ZnO nanowires is in agreement with the red shift observed in the adsorption edge of the DR-UV-Vis spectra. It must be indicated that, in

both cases, the values of the band gaps are in the lower side of the typical range for ZnO nanostructures (from 3.10 eV to 3.40 eV) [72-73].

3.2. Electrochemical and photoelectrochemical characterization

3.2.1. Comparison between ZnO compact layer and nanowires

The photoelectrochemical response of the samples was analyzed by registering the current density versus the applied potential under simulated sunlight on/off conditions (see Figure 8 (a)). For the compact layer, the highest photocurrent density response (calculated as the difference between current density under illumination and current density in the dark) is achieved at -0.22 $V_{Ag/AgCl}$ with a value of 5.81 $\mu A/cm^2$, while for nanowires at this applied potential is 0.33 mA/cm^2. For the nanowires, the highest value of the photocurrent density response is 0.34 mA/cm^2 at -0.38 $V_{Ag/AgCl}$, while it is 4.46 $\mu A/cm^2$ for the compact layer at this applied potential. The higher value of the photocurrent density response for the ZnO nanowires in comparison with the ZnO compact layer might be caused by the morphology in form of nanostructures that increases the specific surface area on the one hand and, on the other hand, by the higher crystallinity that decreases the recombination rate of the photogenerated charge carriers. A photocurrent density value of 0.34 mA cm^{-2} is of the order or even higher than in other studies working with ZnO nanostructures [74-79].

Figure 8 (b-d) shows the PEIS results under illumination for the ZnO nanowires and for the ZnO compact layer, in the form of Nyquist (b), Bode-phase (c) and Bode-modulus (d) plots. Total amplitude of the semicircle/s of the Nyquist plot in the real axis is associated with total resistance. As it can be observed, the amplitude of the Nyquist semicircle/s for the ZnO compact layer is much larger than for the ZnO nanowires, indicating that ZnO nanowires exhibit a lower resistance to charge transfer processes, which is consistent with the higher photocurrent density response in the water splitting test. Likewise, Bode-modulus shows at low frequencies a higher modulus of the impedance for the ZnO compact layer than for the ZnO nanowires, which is related to the total impedance of the system, while the limit at high frequencies, associated with the electrolyte resistance, is similar for both electrodes. On the other hand, the Bode-phase shows one broad peak that is extended over a high range of frequencies for the ZnO compact layer, while the ZnO nanowires presented apparently two peaks. The photoelectrochemical impedance

spectroscopy results for the ZnO nanowires will be studied and analyzed in detail in the following section.

3.2.2. Mott-Schottky analysis of the ZnO nanowires

The semiconductor/electrolyte interface for an n-type semiconductor is described using the following Mott-Schottky equation [80]:

$$\frac{1}{C_{SC}^2} = \frac{1}{C_H^2} + \left(\frac{2}{e \cdot \varepsilon_0 \cdot \varepsilon_r \cdot N_D}\right) \cdot \left(U - U_{FB} - \frac{k \cdot T}{e}\right) \quad (1)$$

where C_{SC} is the space charge layer capacitance, C_H is the Helmholtz layer capacitance, e the electron charge, ε_0 the vacuum permittivity, ε_r the relative dielectric constant of ZnO wurtzite (8.66 [81]), N_D the donor density, U the applied potential, U_{FB} the flat-band potential, k the Boltzmann constant and T the absolute temperature.

Figure 9 shows the Mott–Schottky plots obtained for the ZnO nanowires with and without illumination, marked as light and dark, respectively. For both conditions, a positive slope is showed, which confirms the n-type semiconductor behavior of the ZnO nanowires [19, 82]. The lower slope under illumination indicates a higher electron donor density [83]. The donor density of the ZnO nanowires was calculated from the linear regions of the MS plots, being N_D *(light)*= $1.25 \cdot 10^{20}$ cm^{-3} and N_D *(dark)*= $5.40 \cdot 10^{19}$ cm^{-3}. The value of the donor density under illumination is one order of magnitude higher than in dark conditions. That was expected since under illumination electron/hole pairs are photogenerated which results in the increase of the density of donor species. The high value of the donor density for the ZnO nanowires is consistent with the structural disorders identified in Raman and XPS analysis. Moreover, high donor densities are normally associated with higher conductivities and, thus, higher photoelectrochemical performance [27]. Figure S2 shows that capacitance values are considerably lower for the ZnO compact layer (higher $1/C^2$ values), which is consistent with the impedance results. N_D values calculated for the ZnO compact layer are N_D *(light)*= $1.40 \cdot 10^{19}$ cm^{-3} and N_D *(dark)*= $1.23 \cdot 10^{19}$ cm^{-3}. The decrease in the donor densities for the compact layer in comparison to the ZnO nanowires is associated with a reduction in the electron transport along the oxide. In fact, Mott Schottky plots for the ZnO compact layer obtained with and without illumination present almost the same values, showing a very low photoelectrochemical response for the compact layer.

Calculation of the flat-band potential was performed from the intersection of the straight line in the MS plots with the applied potential axis, presenting values of -0.65 $V_{Ag/AgCl}$ under illumination and -0.64 $V_{Ag/AgCl}$ in the dark.

3.2.2. PEIS study of the charge transfer mechanism for the ZnO nanowires

In order to deeply analyze the photoelectrocatalytic properties of the ZnO nanowires and study the charge transfer mechanism, photoelectrochemical impedance spectroscopy analyses at different applied potentials (*vs.* Ag/AgCl) under simulated solar light AM 1.5 were performed.

Figure 10 shows the Bode-phase (a) and Nyquist (b) plots at applied potentials near the flat band potential. In the Bode-phase plot at more negative potentials than the flat-band potential, i.e -0.8 and -0.7 $V_{Ag/AgCl}$, one single peak at intermediate-low frequencies is noticed. This peak denotes a non-ideal capacitive behavior, given by the high value of the phase angle, which is around 70 degrees. When the applied potential becomes less negative (around the flat band value) this peak gradually disappears, shifting to lower frequencies as the potential becomes less negative. Simultaneously, when the applied potential overcomes the flat band potential (from -0.6 V onwards), one peak at intermediate frequencies followed by other peak at high frequencies appear, reaching higher phase angle values (and shifting to higher frequencies) when applying less negative potentials. That is in accordance with Nyquist plots where one single semicircle is observed at -0.8 and -0.7 $V_{Ag/AgCl}$, while three semicircles are observed when increasing the applied potential to less negative potentials: (i) a small one at high frequencies located on the left side of the Nyquist plots (see inset of Figure 10 (b)), (ii) at intermediate frequencies and (iii) at high frequencies located on the right side of the Nyquist plot. The amplitude of the semicircle located at high frequencies does not seem to experiment variations within the potential range, while the amplitude of the semicircle located at intermediate frequencies decreases by increasing the applied potential until reaching its minimum at -0.50 $V_{Ag/AgCl}$ and then increases again, as it will be explained when describing Figure 11.

Additionally, Figure 11 shows the Bode-phase (a) and Nyquist (b) plots obtained at higher (more positive) applied potentials. In the Bode-phase plot, two peaks at intermediate and high frequencies are observed in all the potential range, which experiment different variations with potential. On the other hand, in the Nyquist plot two phenomena are

noticed: the amplitude of the semicircle at high frequencies decreases until reaching the minimum at -0.25 $V_{Ag/AgCl}$, while the amplitude of the semicircle at intermediate frequencies reaches its minimum near the flat band potential and increases when moving the potential to less negative values.

According to the results and the literature [2], recombination and charge transfer processes are described by the assumption of the equivalent circuit of Figure 12, in which three time constants (RC) are included. In this circuit, Constant Phase Elements (CPE) were used instead of pure capacitors, to consider the non-ideality of the system. The parameter α associated with each CPE indicates the deviation from the ideality (the CPE is considered as a pure capacitor when α = 1 and a pure resistor when α =0). The experimental data from PEIS measurements were fitted to the equivalent circuit by using Zview software in which values of χ^2 in the order of 10^{-3}-10^{-4} were obtained. R_S is the resistance associated with the electrolyte and keeps constant within the potential range with a value of $\approx 7\ \Omega \cdot cm^2$, which is showed in the Nyquist plots from Figure 10 (b) and 11 (b). The time constant corresponding to R_3 and $C3$ is related to some process which disappears when increasing the applied potential beyond the flat band potential, as observed at low frequencies in Figure 10 (a) and Figure 11 (a). Therefore, it might be related to charge transfer processes whose impedance disappears when increasing the applied potential and, thus, it does not interfere with the global process at potentials more positive than U_{FB}. Additionally, the time constant associated with R_1 and C_1, showed at high frequencies of Figure 10 and Figure 11, corresponds to the electron-hole recombination, while the time constant associated with R_2 and C_2 is related to the charge transfer of holes [2]. More specifically, R_1 corresponds to recombination resistance of electrons going from the conduction band to the valence band or the surface states and C_1 is the chemical capacitance associated with the free electrons in the conduction band [2]. Likewise, R_2 is related to the hole transfer resistance and C_2 is the chemical capacitance of the surface states or the valence band [2].

With the aim of evaluating whether the charge transfer of holes at the semiconductor/electrolyte interface occurs directly from the valence band or indirectly via surface states, the variation of the charge transfer capacitance (C_2) versus the applied potential was studied. Since the potential dependence for both charge transfer mechanisms is clearly different, the variation of the capacitance with the potential is a powerful tool to differentiate between direct and indirect charge transfer [7]. The charge

transfer capacitance (C_2) was calculated by using Brug's expression [84] (equation 2), where values of CPE_2, α_2 and R_2 were obtained from Zview analysis.

$$C_2 = CPE_2^{\left(\frac{1}{\alpha_2}\right)} \cdot R_2^{\frac{(1-\alpha_2)}{\alpha_2}} \quad (2)$$

Figure 13 shows the charge transfer capacitance versus the applied potential (Ag/AgCl). As it can be observed, the capacitance changes with the potential showing the form of a peak, which is characteristic of the charge transfer of holes via surface states [7, 9, 85, 86]. This peak indicates the transition between the surface states filled with electrons (occupied) and the surface states filled with holes (unoccupied) [7].

For the charge transfer of holes via surface states, the holes originated when the ZnO photoanode is illuminated are trapped in the surface states. Subsequently, these holes can participate in electrolyte oxidation (Figure S3) or recombine with the electrons trapped in the surface states [36]. Higher photocurrent densities are reached when population of trapped electron decreases and, thus, surface state electron-hole recombination decreases. Bisquert et al. [7] showed that current densities in a photoelectrocatalytic process, such as hydrogen production by photoelectrochemical water splitting, might be higher if the charge transfer takes place via surface states instead of taking place from the valence band. The current density achieved via surface state charge transfer is originated by the extraction of the electrons present in surface states, which can be produced by the capture of the photogenerated holes or by the injection of electrons from the surface states to the conduction band by applying an anodic bias. Consequently, the current density from charge transfer via surface states is originated from both charge carriers photogeneration and the applied bias and, thus, it can be higher than it is if charge transfer is produced from the valence band. In addition, it was demonstrated that onset voltage can be lower in the presence of surface states due to an enhancement in the kinetics of the charge transfer [7,37]. For these reasons, surface states could be an interesting feature in semiconductor design for photoelectrocatalytic applications, such as hydrogen production, since they promote charge separation and UV-Vis light harvesting and act as fast hole transport mechanism that enhances oxygen evolution kinetics for photoelectrochemical water splitting [87]. Hence, what is important in this work is to identify that the main interfacial charge transfer mechanism of ZnO nanowires upon illumination is mediated by surface states, regardless of the precise nature or the specific properties of these surface states on the ZnO nanowires surface. Knowing the charge

transfer mechanism between the illuminated photoanode and the electrolyte will subsequently permit the design and modification of nanostructures. Obviously, further analyses on the characteristics of surface states are important to engineer nanostructures in order to enhance their photoelectrocatalytic performance, but results obtained in this work represent an important step in that way.

4. Conclusions

High aspect ratio ZnO nanowires were formed by simple anodization (10 V/ 10 min) and subsequent thermal annealing (300 ºC/ 1 hour). Besides, the synthesized electrodes presented high roughness, as observed from high values of Sa in the atomic force microscopy. TEM and HRTEM analyses confirmed the porosity of the nanowires synthesized as well as the only presence of the wurtzite ZnO structure.

From XRD and Raman study, it can be stated that ZnO nanowires presented hexagonal wurtzite structure with high crystallinity after annealing. Likewise, matrix elements of ZnO wurtzite structure formed by Zn–O bonds were observed through XPS. Furthermore, the ZnO nanowires were oriented preferentially along the (101) plane, as shown in XRD analysis. From the DR-UV-Vis. spectra it can be concluded that the absorbance of ZnO nanowires is higher and the bandgap energy slightly lower than those of the ZnO compact layer.

In addition, phonon modes associated with defects in the crystalline structure, such as oxygen vacancies and zinc interstitial, were identified in the Raman spectra. Similarly, oxygen chemical states in XPS unveiled the presence of surface structural disorders, i.e., oxygen vacancies and hydroxyl groups, that could act as energy levels within the valence band and the conduction band. These results are in concordance with the high donor density calculated from Mott-Schottky analysis, with values of $5.40 \cdot 10^{19}$ cm^{-3} and $1.25 \cdot 10^{20}$ cm^{-3} in dark and simulated solar light conditions, respectively.

From a photoelectrochemical point of view, the ZnO nanowires presented better results than the ZnO compact layer. In particular, the former exhibit good photosensibility in the photoelectrochemical test, presenting photocurrent densities 85 times higher than the compact layer (at an applied potential of -0.38 $V_{Ag/AgCl}$). Similarly, PEIS results showed that the resistance to charge transfer in the ZnO nanowires was much lower than in the

ZnO compact layer, which is attributed to the nanostructured morphology and their higher crystallinity.

Finally, the study of the charge transfer capacitance versus the applied potential through the PEIS technique showed that the charge transfer mechanism in the ZnO nanowires occurs indirectly via surface states. The knowledge of the nature of charge transfer processes at the interface upon illuminating the ZnO photoanodes is very valuable to improve their photoelectrocatalytic performance through nanotechnology.

Acknowledgements

Authors would like to express their gratitude to the Generalitat Valenciana and to the European Social Fund for their financial support within the subvention GJIDI/2018/A/067. Authors also thank to project co-funded by FEDER operational programme 2014-2020 of Comunitat Valenciana (IDIFEDER/18/044). Finally, authors thank to Ministerio de Ciencia e Innovación- Agencia Estatal de Investigación (PID2019-105844RB-I00/AEI/10.13039/501100011033) and MINECO for its help in the Laser Raman Microscope acquisition (UPOV08-3E-012) co-financed by the European Social Fund. Authors would also like to express their gratitude for the financial support to the "Generalitat Valenciana (GV/2021/011). Authors also thanks MINECO for MAT2017-84118-C2-1-R MCIN/AEI/10.13039/501100011033/ project and FEDER Una manera de hacer Europa.

Data availability

The raw/processed data required to reproduce these findings cannot be shared at this time due to technical or time limitations.

References

[1] A. Kudo, Y. Miseki, Heterogeneous photocatalyst materials for water splitting, Chem. Soc. Rev. 38 (2009) 253–278. https://doi.org/10.1039/b800489g.

[2] L. Bertoluzzi, J. Bisquert, Equivalent circuit of electrons and holes in thin

semiconductor films for photoelectrochemical water splitting applications, J. Phys. Chem. Lett. 3 (2012) 2517–2522. https://doi.org/10.1021/jz3010909.

[3] J. Li, N. Wu, Semiconductor-based photocatalysts and photoelectrochemical cells for solar fuel generation: A review, Catal. Sci. Technol. 5 (2015) 1360–1384. https://doi.org/10.1039/c4cy00974f.

[4] M.A.M. Al-Alwani, A.B. Mohamad, N.A. Ludin, A.A.H. Kadhum, K. Sopian, Dye-sensitised solar cells: Development, structure, operation principles, electron kinetics, characterisation, synthesis materials and natural photosensitisers, Renew. Sustain. Energy Rev. 65 (2016) 183–213. https://doi.org/10.1016/j.rser.2016.06.045.

[5] N.S. Lewis, Toward cost-effective solar energy use, Science (80-.). 315 (2007) 798–801. https://doi.org/10.1126/science.1137014.

[6] C. Acar, I. Dincer, A review and evaluation of photoelectrode coating materials and methods for photoelectrochemical hydrogen production, Int. J. Hydrogen Energy. 41 (2016) 7950–7959. https://doi.org/10.1016/j.ijhydene.2015.11.160.

[7] L. Bertoluzzi, P. Lopez-Varo, J.A. Jiménez Tejada, J. Bisquert, Charge transfer processes at the semiconductor/electrolyte interface for solar fuel production: Insight from impedance spectroscopy, J. Mater. Chem. A. 4 (2016) 2873–2879. https://doi.org/10.1039/c5ta03210e.

[8] V. Cristino, S. Marinello, A. Molinari, S. Caramori, S. Carli, R. Boaretto, R. Argazzi, L. Meda, C.A. Bignozzi, Some aspects of the charge transfer dynamics in nanostructured WO3 films, J. Mater. Chem. A. 4 (2016) 2995–3006. https://doi.org/10.1039/c5ta06887h.

[9] B. Klahr, S. Gimenez, F. Fabregat-Santiago, T. Hamann, J. Bisquert, Water oxidation at hematite photoelectrodes: The role of surface states, J. Am. Chem. Soc. 134 (2012) 4294–4302. https://doi.org/10.1021/ja210755h.

[10] A. Fujishima, K. Honda, Electrochemical photolysis of water at a semiconductor electrode, Nature. 238 (1972) 37–38. https://doi.org/10.1038/238037a0.

[11] S. Hernández, D. Hidalgo, A. Sacco, A. Chiodoni, A. Lamberti, V. Cauda, E. Tresso, G. Saracco, Comparison of photocatalytic and transport properties of TiO2

and ZnO nanostructures for solar-driven water splitting, Phys. Chem. Chem. Phys. 17 (2015) 7775–7786. https://doi.org/10.1039/c4cp05857g.

[12] R. van de Krol, M. Grätzel, Photoelectro - chemical Hydrogen Production, Springer, 2012. https://doi.org/10.10007/978-1-4614-1380-6.

[13] P.S. Archana, R. Jose, C. Vijila, S. Ramakrishna, Improved electron diffusion coefficient in electrospun TiO2 nanowires, J. Phys. Chem. C. 113 (2009) 21538–21542. https://doi.org/10.1021/jp908238q.

[14] A. Kolodziejczak-Radzimska, T. Jesionowski, Zinc oxide-from synthesis to application: A review, Materials (Basel). 7 (2014) 2833–2881. https://doi.org/10.3390/ma7042833.

[15] Y. Ji, One-step method for growing of large scale ZnO nanowires on zinc foil, Mater. Lett. 138 (2015) 92–95. https://doi.org/10.1016/j.matlet.2014.09.095.

[16] L. Liu, W. Wang, J. Long, S. Fu, Y. Liang, J. Fu, Three-dimensional plasmonic photoanode of Au nanoparticles/ZnFe 2 O 4 nanosheets coated onto ZnO nanotube arrays for photoelectrochemical production of hydrogen, Sol. Energy Mater. Sol. Cells. 195 (2019) 330–338. https://doi.org/10.1016/j.solmat.2019.03.028.

[17] C. Florica, N. Preda, A. Costas, I. Zgura, I. Enculescu, ZnO nanowires grown directly on zinc foils by thermal oxidation in air: Wetting and water adhesion properties, Mater. Lett. 170 (2016) 156–159. https://doi.org/10.1016/j.matlet.2016.02.035.

[18] S. Farhad, N. Tanvir, M. Bashar, M. Hossain, M. Sultana, N. Khatun, Facile synthesis of oriented zinc oxide seed layer for the hydrothermal growth of zinc oxide nanorods, Bangladesh J. Sci. Ind. Res. 53 (2018) 233–244. https://doi.org/10.3329/bjsir.v53i4.39186.

[19] M.C. Huang, T. Wang, B.J. Wu, J.C. Lin, C.C. Wu, Anodized ZnO nanostructures for photoelectrochemical water splitting, Appl. Surf. Sci. 360 (2016) 442–450. https://doi.org/10.1016/j.apsusc.2015.09.174.

[20] P. Batista-Grau, R. Sánchez-Tovar, R.M. Fernández-Domene, J. García-Antón, Formation of ZnO nanowires by anodization under hydrodynamic conditions for photoelectrochemical water splitting, Surf. Coat. Technol. 381 (2020) 125197.

https://doi.org/10.1016/j.surfcoat.2019.125197.

[21] A. Di Mauro, M.E. Fragalà, V. Privitera, G. Impellizzeri, ZnO for application in photocatalysis: From thin films to nanostructures, Mater. Sci. Semicond. Process. 69 (2017) 44–51. https://doi.org/10.1016/j.mssp.2017.03.029.

[22] S. He, M. Zheng, L. Yao, X. Yuan, M. Li, L. Ma, W. Shen, Preparation and properties of ZnO nanostructures by electrochemical anodization method, Appl. Surf. Sci. 256 (2010) 2557–2562. https://doi.org/10.1016/j.apsusc.2009.10.104.

[23] H. Tong, S. Ouyang, Y. Bi, N. Umezawa, M. Oshikiri, J. Ye, Nano-photocatalytic materials: Possibilities and challenges, Adv. Mater. 24 (2012) 229–251. https://doi.org/10.1002/adma.201102752.

[24] P. Batista-Grau, R.M. Fernández-Domene, R. Sánchez-Tovar, J. García-Antón, Control on the morphology and photoelectrocatalytic properties of ZnO nanostructures by simple anodization varying electrolyte composition, J. Electroanal. Chem. 880 (2021) 114933. https://doi.org/10.1016/j.jelechem.2020.114933.

[25] A. Sanz-Marco, R. Sánchez-Tovar, M.M. Bajo, R.M. Fernández-Domene, J. García-Antón, Cathodoluminescence characterization of ZnO/ZnS nanostructures anodized under hydrodynamic conditions, Electrochim. Acta. 269 (2018) 553–559. https://doi.org/10.1016/j.electacta.2018.03.046.

[26] X.-C. Dai, S. Hou, M.-H. Huang, Y.-B. Li, T. Li, F.-X. Xiao, Electrochemically anodized one-dimensional semiconductors: a fruitful platform for solar energy conversion, J. Phys. Energy. 1 (2019) 022002. https://doi.org/10.1088/2515-7655/ab0718.

[27] B. Lucas-Granados, R. Sánchez-Tovar, R.M. Fernández-Domene, J. García-Antón, Study of the annealing conditions and photoelectrochemical characterization of a new iron oxide bi-layered nanostructure for water splitting, Sol. Energy Mater. Sol. Cells. 153 (2016) 68–77. https://doi.org/10.1016/j.solmat.2016.04.005.

[28] P. Batista-Grau, R. Sánchez-Tovar, R.M. Fernández-Domene, J. García-Antón, ZnO nanostructures: Synthesis by anodization and applications in photoelectrocatalysis, Rev. Chem. Eng. 2010 (2021) 1–24.

https://doi.org/10.1515/revce-2020-0110.

[29] L. Zaraska, K. Mika, K. Syrek, G.D. Sulka, Formation of ZnO nanowires during anodic oxidation of zinc in bicarbonate electrolytes, J. Electroanal. Chem. 801 (2017) 511–520. https://doi.org/10.1016/j.jelechem.2017.08.035.

[30] C.F. Mah, K.P. Beh, F.K. Yam, Z. Hassan, Rapid Formation and Evolution of Anodized-Zn Nanostructures in NaHCO3 Solution, ECS J. Solid State Sci. Technol. 5 (2016) M105–M112. https://doi.org/10.1149/2.0061610jss.

[31] R. Sánchez-Tovar, R.M. Fernández-Domene, M.T. Montañés, A. Sanz-Marco, J. Garcia-Antón, ZnO/ZnS heterostructures for hydrogen production by photoelectrochemical water splitting, RSC Adv. 6 (2016) 30425–30435. https://doi.org/10.1039/c6ra03501a.

[32] R.M. Fernández-Domene, R. Sánchez-Tovar, B. Lucas-Granados, J. García-Antón, Principios de fotoelectroquímica, Valencia, Universitat Politècnica de València, 2018.

[33] H. Ge, H. Tian, Y. Zhou, S. Wu, D. Liu, X. Fu, X.M. Song, X. Shi, X. Wang, N. Li, Influence of surface states on the evaluation of the flat band potential of TiO2, ACS Appl. Mater. Interfaces. 6 (2014) 2401–2406. https://doi.org/10.1021/am404743a.

[34] W.H. Leng, Z. Zhang, J.Q. Zhang, C.N. Cao, Investigation of the kinetics of a TiO2 photoelectrocatalytic reaction involving charge transfer and recombination through surface states by electrochemical impedance spectroscopy, J. Phys. Chem. B. 109 (2005) 15008–15023. https://doi.org/10.1021/jp051821z.

[35] D.K. Chakrabarty, Solid Surface, in: Solid State Chem., New Academic Science, 2010.

[36] Y. Hu, F. Boudoire, I. Hermann-Geppert, P. Bogdanoff, G. Tsekouras, B.S. Mun, G. Fortunato, M. Graetzel, A. Braun, Molecular Origin and Electrochemical Influence of Capacitive Surface States on Iron Oxide Photoanodes, J. Phys. Chem. C. 120 (2016) 3250–3258. https://doi.org/10.1021/acs.jpcc.5b08013.

[37] S. Kumar, K. Ojha, A.K. Ganguli, Interfacial Charge Transfer in Photoelectrochemical Processes, Adv. Mater. Interfaces. 4 (2017).

https://doi.org/10.1002/admi.201600981.

[38] A. Das, R.G. Nair, Effect of aspect ratio on photocatalytic performance of hexagonal ZnO nanorods, J. Alloys Compd. 817 (2020) 153277. https://doi.org/10.1016/j.jallcom.2019.153277.

[39] Z. Hu, Q. Chen, Z. Li, Y. Yu, L.M. Peng, Large-scale and rapid synthesis of ultralong ZnO nanowire films via anodization, J. Phys. Chem. C. 114 (2010) 881–889. https://doi.org/10.1021/jp9094744.

[40] J. Park, K. Kim, J. Choi, Formation of ZnO nanowires during short durations of potentiostatic and galvanostatic anodization, Curr. Appl. Phys. 13 (2013) 1370–1375. https://doi.org/10.1016/j.cap.2013.04.015.

[41] D.O. Miles, P.J. Cameron, D. Mattia, Hierarchical 3D ZnO nanowire structures via fast anodization of zinc, J. Mater. Chem. A. 3 (2015) 17481–17882. https://doi.org/10.1039/c5ta03578c.

[42] R. Sánchez-Tovar, E. Blasco-Tamarit, R.M. Fernández-Domene, M. Villanueva-Pascual, J. García-Antón, Electrochemical formation of novel TiO2-ZnO hybrid nanostructures for photoelectrochemical water splitting applications, Surf. Coatings Technol. 388 (2020) 125605. https://doi.org/10.1016/j.surfcoat.2020.125605.

[43] A.Y. Faid, N.K. Allam, Stable solar-driven water splitting by anodic ZnO nanotubular semiconducting photoanodes, RSC Adv. 6 (2016) 80221–80225. https://doi.org/10.1039/c6ra18747a.

[44] A. Khan, N. Sciences, Raman Spectroscopic Study of the ZnO Nanostructures Raman Spectroscopic Study of the ZnO Nanostructures, J Pak Mater Soc. 4 (1) (2010) 5–9.

[45] T.C. Damen, S.P.S. Porto, B. Tell, Raman Effect in Zinc Oxide, Phys. Rev. 142 (1966) 570–574.

[46] A.K. Bhunia, P.K. Jha, D. Rout, S. Saha, Morphological Properties and Raman Spectroscopy of ZnO Nanorods, J. Phys. Sci. 21 (2016) 111–118.

[47] J. Das, S.K. Pradhan, D.R. Sahu, D.K. Mishra, S.N. Sarangi, B.B. Nayak, S. Verma, B.K. Roul, Micro-Raman and XPS studies of pure ZnO ceramics, Phys. B

Condens. Matter. 405 (2010) 2492–2497. https://doi.org/10.1016/j.physb.2010.03.020.

[48] R. Ghosh, S. Kundu, R. Majumder, M.P. Chowdhury, Hydrothermal synthesis and characterization of multifunctional ZnO nanomaterials, Mater. Today Proc. 26 Part 1 (2019) 77–81. https://doi.org/10.1016/j.matpr.2019.04.217.

[49] X.Q. Wei, B.Y. Man, M. Liu, C.S. Xue, H.Z. Zhuang, C. Yang, Blue luminescent centers and microstructural evaluation by XPS and Raman in ZnO thin films annealed in vacuum, N2 and O2, Phys. B Condens. Matter. 388 (2007) 145–152. https://doi.org/10.1016/j.physb.2006.05.346.

[50] J. Wang, Z. Wang, B. Huang, Y. Ma, Y. Liu, X. Qin, X. Zhang, Y. Dai, Oxygen vacancy induced band-gap narrowing and enhanced visible light photocatalytic activity of ZnO, ACS Appl. Mater. Interfaces. 4 (2012) 4024–4030. https://doi.org/10.1021/am300835p.

[51] N.K. Shrestha, K. Lee, R. Hahn, P. Schmuki, Corrigendum to ‘Anodic growth of hierarchically structured nanotubular ZnO architectures on zinc surfaces using a sulfide based electrolyte’ [Electrochemistry Communications 34 (2013) 9–13], Electrochem. Commun. 34 (2013) 361. https://doi.org/10.1016/j.elecom.2013.07.003.

[52] A.R. Marlinda, N. Yusoff, A. Pandikumar, N.M. Huang, O. Akbarzadeh, S. Sagadevan, Y.A. Wahab, M.R. Johan, Tailoring morphological characteristics of zinc oxide using a one-step hydrothermal method for photoelectrochemical water splitting application, Int. J. Hydrogen Energy. 44 (2019) 17535–17543. https://doi.org/10.1016/j.ijhydene.2019.05.109.

[53] A. Saranya, T. Devasena, H. Sivaram, R. Jayavel, Materials Science in Semiconductor Processing Role of hexamine in ZnO morphologies at different growth temperature with potential application in dye sensitized solar cell, Mater. Sci. Semicond. Process. 92 (2019) 108–115. https://doi.org/10.1016/j.mssp.2018.03.028.

[54] L. Zaraska, K. Mika, K.E. Hnida, M. Gajewska, T. Łojewski, M. Jaskuła, G.D. Sulka, High aspect-ratio semiconducting ZnO nanowires formed by anodic oxidation of Zn foil and thermal treatment, Mater. Sci. Eng. B Solid-State Mater.

Adv. Technol. 226 (2017) 94–98. https://doi.org/10.1016/j.mseb.2017.09.003.

[55] P.R. Deshmukh, Y. Sohn, W.G. Shin, Chemical synthesis of ZnO nanorods: Investigations of electrochemical performance and photo-electrochemical water splitting applications, J. Alloys Compd. 711 (2017) 573–580. https://doi.org/10.1016/j.jallcom.2017.04.030.

[56] N. Samir, D.S. Eissa, N.K. Allam, Self-assembled growth of vertically aligned ZnO nanorods for light sensing applications, Mater. Lett. 137 (2014) 45–48. https://doi.org/10.1016/j.matlet.2014.08.114.

[57] A. Ievtushenko, O. Khyzhun, I. Shtepliuk, V. Tkach, V. Lazorenko, G. Lashkarev, X-ray photoelectron spectroscopy study of nitrogen and aluminum-nitrogen doped ZnO films, Acta Phys. Pol. A. 124 (5) (2013) 858–861. https://doi.org/10.12693/APhysPolA.124.858.

[58] C.D. Wagner, W.M. Riggs, L.E. Davis, J.F. Moulder, G.E. Muilenberg, Handbook of X-ray electron spectroscopy, 1979.

[59] D. Briggs, Surface analysis, in: Handb. Adhes. Second Ed., 2005. https://doi.org/10.1002/0470014229.ch17.

[60] S. Maroie, G. Haemers, J.J. Verbist, Surface oxidation of polycrystalline α(75%Cu/25%Zn) and β(53%Cu/47%Zn) brass as studied by XPS: Influence of oxygen pressure, Appl. Surf. Sci. 17 (1984) 463–467. https://doi.org/10.1016/0378-5963(84)90006-0.

[61] J.H. Zheng, Q. Jiang, J.S. Lian, Synthesis and optical properties of flower-like ZnO nanorods by thermal evaporation method, Appl. Surf. Sci. 217 (2011) 5083–5087. https://doi.org/10.1016/j.apsusc.2011.01.025.

[62] F. Meng, F. Ge, Y. Chen, G. Xu, F. Huang, Surface & Coatings Technology Local structural changes induced by ion bombardment in magnetron sputtered ZnO : Al films : Raman , XPS , and XAS study, Surf. Coat. Technol. 365 (2019) 2–9. https://doi.org/10.1016/j.surfcoat.2018.04.013.

[63] Z. Wu, S. Tyan, H. Chen, Superlattices and Microstructures Temperature-dependent photoluminescence and XPS study of ZnO nanowires grown on fl exible Zn foil via thermal oxidation, Superlattices Microstruct. 107 (2017) 38–43.

https://doi.org/10.1016/j.spmi.2017.04.016.

[64] N. Kamarulzaman, M.F. Kasim, N.F. Chayed, Results in Physics Elucidation of the highest valence band and lowest conduction band shifts using XPS for ZnO and Zn 0 . 99 Cu 0 . 01 O band gap changes, Results Phys. 6 (2016) 217–230. https://doi.org/10.1016/j.rinp.2016.04.001.

[65] T.G.G. Maffeis, M.W. Penny, A. Castaing, O.J. Guy, S.P. Wilks, Surface Science XPS investigation of vacuum annealed vertically aligned ultralong ZnO nanowires, Surf. Sci. 606 (2012) 99–103. https://doi.org/10.1016/j.susc.2011.09.007.

[66] X. Zhang, J. Qin, Y. Xue, P. Yu, B. Zhang, L. Wang, R. Liu, Effect of aspect ratio and surface defects nanorods, Scientific Reports 4 (2014) 4596. https://doi.org/10.1038/srep04596.

[67] R. Al-Gaashani, S. Radiman, A.R. Daud, N. Tabet, Y. Al-Douri, XPS and optical studies of different morphologies of ZnO nanostructures prepared by microwave methods, Ceram. Int. 39 (2013) 2283–2292. https://doi.org/10.1016/j.ceramint.2012.08.075.

[68] F. Chang, S. Brahma, J. Huan, Z. Wu, K. Lo, Strong correlation between optical properties and mechanism in deficiency of normalized self- assembly ZnO nanorods, (2019) 1–9. https://doi.org/10.1038/s41598-018-37601-8.

[69] Z. Wang , X.-F. Qian , J. Yin and Z.-K. Zhu. Large-Scale Fabrication of Tower-Like, Flower-Like, and Tube-Like ZnO Arrays by a Simple Chemical Solution Route. Langmuir, 20 (2004) 3441-3448. http://dx.doi.org/10.1021/la036098.

[70] J. Tauc, R. Grigorovici, A. Vancu. Optical Properties and Electronic Structure of Amorphous Germanium. Physica Status Solidi B. 15 (1966) 627-637. https://doi.org/10.1002/pssb.19660150224.

[71] N. F. Mott, E.A. Davis. Electronic Processes in Non-Crystalline Materials (2012); OUP Oxford.

[72] Kl. Davis, R. Yarbrough, M, Froeschle, J. White an H. Rathnayake, Band gap engineered zinc oxide nanostructures via a sol–gel synthesis of solvent driven shape-controlled crystal growth, RSC Adv., 2019,9, 14638-14648. https://doi.org/10.1039/C9RA02091H.

[73] D. Guo, J. Wang, C. Cui, P. Li, X. Zhong, F. Wang, S. Yuan, K. Zhang, Y. Zhou. ZnO@ TiO_2 core–shell nanorod arrays with enhanced photoelectrochemical performance. Solar Energy, 95 (2013) 237-245. https://doi.org/10.1016/j.solener.2013.06.003.

[74] S. Guo, X. Zhao, W. Zhang, W. Wang, Optimization of electrolyte to significantly improve photoelectrochemical water splitting performance of ZnO nanowire arrays, Mater. Sci. Eng. B Solid-State Mater. Adv. Technol. 227 (2018) 129–135. https://doi.org/10.1016/j.mseb.2017.09.020.

[75] Y. Lan, Z. Liu, Z. Guo, X. Li, L. Zhao, L. Zhan, M. Zhang, A ZnO/ZnFe2O4 uniform core-shell heterojunction with a tubular structure modified by NiOOH for efficient photoelectrochemical water splitting, Dalt. Trans. 47 (2018) 12181–12187. https://doi.org/10.1039/c8dt02581a.

[76] H.Q. Huynh, K.N. Pham, B.T. Phan, C.K. Tran, H. Lee, V.Q. Dang, Enhancing visible-light-driven water splitting of ZnO nanorods by dual synergistic effects of plasmonic Au nanoparticles and Cu dopants, J. Photochem. Photobiol. A Chem. 399 (2020) 112639. https://doi.org/10.1016/j.jphotochem.2020.112639.

[77] M. Wu, W.J. Chen, Y.H. Shen, F.Z. Huang, C.H. Li, S.K. Li, In situ growth of matchlike ZnO/Au plasmonic heterostructure for enhanced photoelectrochemical water splitting, ACS Appl. Mater. Interfaces. 6 (2014) 15052–15060. https://doi.org/10.1021/am503044f.

[78] Y. Liu, X. Yan, Z. Kang, Y. Li, Y. Shen, Y. Sun, L. Wang, Y. Zhang, Synergistic Effect of Surface Plasmonic particles and Surface Passivation layer on ZnO Nanorods Array for Improved Photoelectrochemical Water Splitting, Sci. Rep. 6 (2016) 1–7. https://doi.org/10.1038/srep29907.

[79] Y. Qiu, K. Yan, H. Deng, S. Yang, Secondary branching and nitrogen doping of ZnO nanotetrapods: Building a highly active network for photoelectrochemical water splitting, Nano Lett. 12 (2012) 407–413. https://doi.org/10.1021/nl2037326.

[80] Q. Zhang, Y. Huang, S. Peng, Y. Zhang, Z. Shen, J. ji Cao, W. Ho, S.C. Lee, D.Y.H. Pui, Perovskite LaFeO3-SrTiO3 composite for synergistically enhanced NO removal under visible light excitation, Appl. Catal. B Environ. 204 (2017) 346–357. https://doi.org/10.1016/j.apcatb.2016.11.052.

[81] Z. Fan, J.G. Lu, Zinc oxide nanostructures: Synthesis and properties, J. Nanosci. Nanotechnol. 5 (2005) 1561–1573. https://doi.org/10.1166/jnn.2005.182.

[82] R.M. Fernández-Domene, R. Sánchez-Tovar, B. Lucas-Granados, J. García-Antón, Improvement in photocatalytic activity of stable WO_3 nanoplatelet globular clusters arranged in a tree-like fashion: Influence of rotation velocity during anodization, Appl. Catal. B Environ. 189 (2016) 266–282. https://doi.org/10.1016/j.apcatb.2016.02.065.

[83] B. Lucas-Granados, R. Sánchez-Tovar, R.M. Fernández-Domene, J.M. Estívalis-Martínez, J. García-Antón, How does anodization time affect morphological and photocatalytic properties of iron oxide nanostructures?, J. Mater. Sci. Technol. 38 (2020) 159–169. https://doi.org/10.1016/j.jmst.2019.07.046.

[84] G.J. Brug, A.L.G. Van Deen Eeden, M. Sluyters-Rehbach, J.H. Sluyters, The analysis of electrode impedances complicated by the presence of a constant phase element, J. Electroanal. Chem. 176 (1984) 275–295.

[85] G. Oskam, P.M. Hoffmann, P.C. Searson, In situ measurements of interface states at silicon surfaces in fluoride solutions, Phys. Rev. Lett. 76 (1996) 1521–1524. https://doi.org/10.1103/PhysRevLett.76.1521.

[86] P.Y. Tang, J. Arbiol, Engineering surface states of hematite based photoanodes for boosting photoelectrochemical water splitting, Nanoscale Horizons. 4 (2019) 1256–1276. https://doi.org/10.1039/c9nh00368a.

[87] T. Zhou, J. Wang, Y. Zhang, C. Zhou, J. Bai, J. Li, B.Zhou, Oxygen vacancy-abundant carbon quantum dots as superfast hole transport channel for vastly improving surface charge transfer efficiency of $BiVO_4$ photoanode, Chem. Eng. J. 431 (2022) 133414. https://doi.org/10.1016/j.cej.2021.133414.

Figures

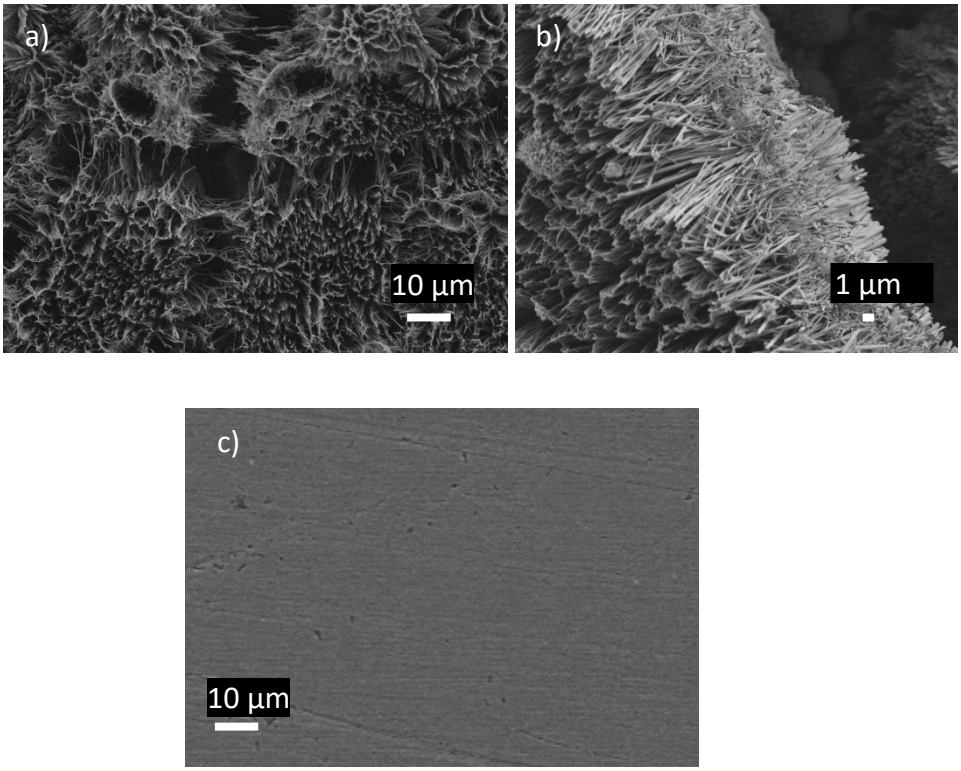

Figure 1. FESEM image of the ZnO nanowires: top (a) and cross-section (b) view. (c) ZnO compact layer.

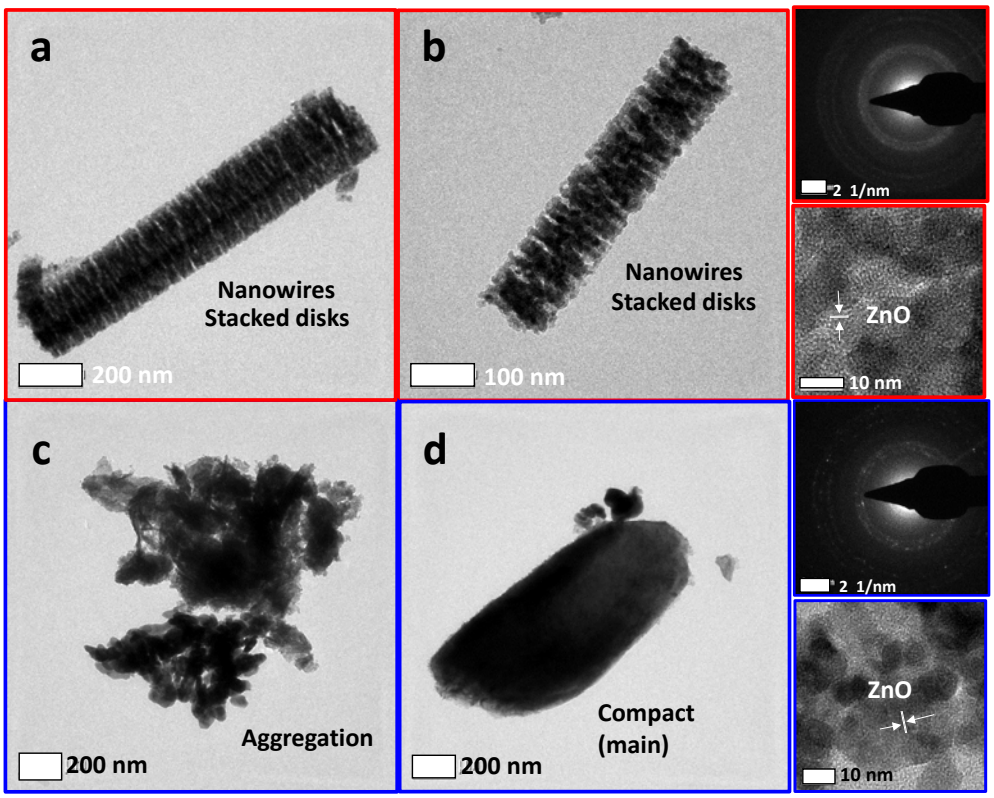

Figure 2. TEM image of the ZnO nanowires (a,b) and ZnO compact layer (c,d). The corresponding HRTEM images of both samples are presented to the right of the figures.

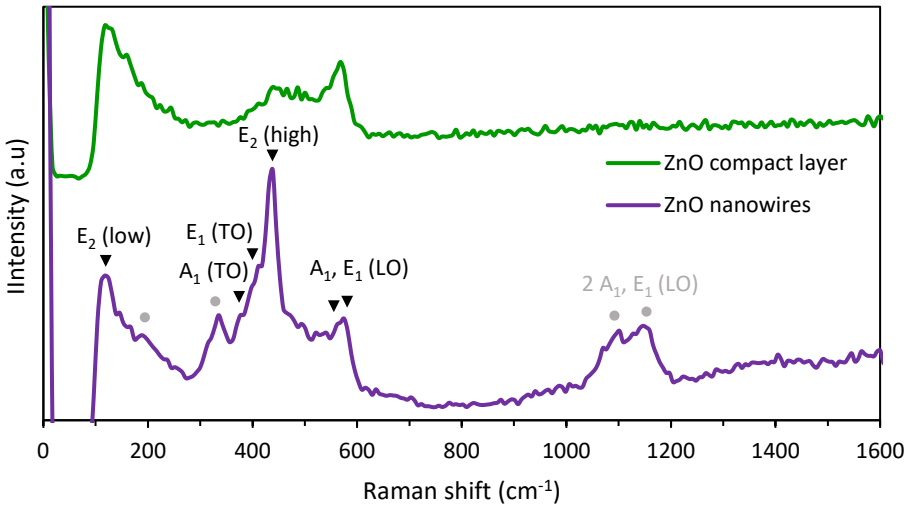

Figure 3. Raman spectra of the ZnO samples. The peaks identification markers correspond to ZnO wurtzite structure first order (dark triangles) and second order (gray light circles) Raman modes.

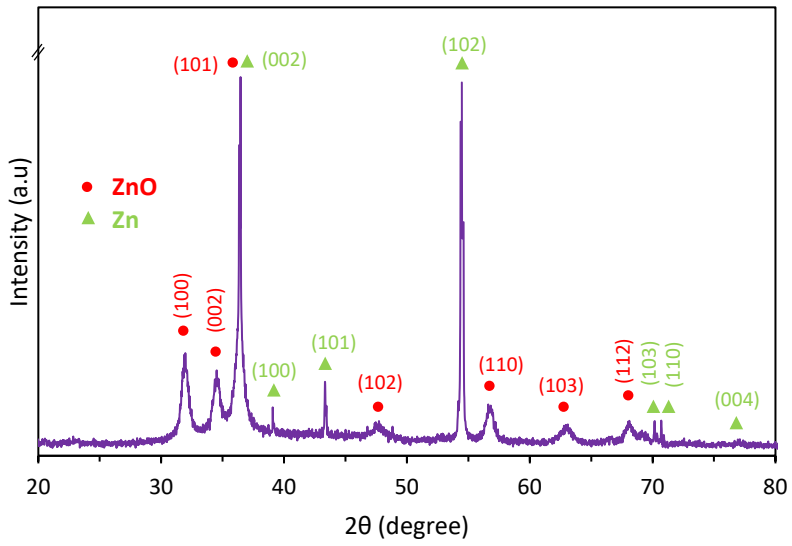

Figure 4. XRD pattern of the ZnO nanowires.

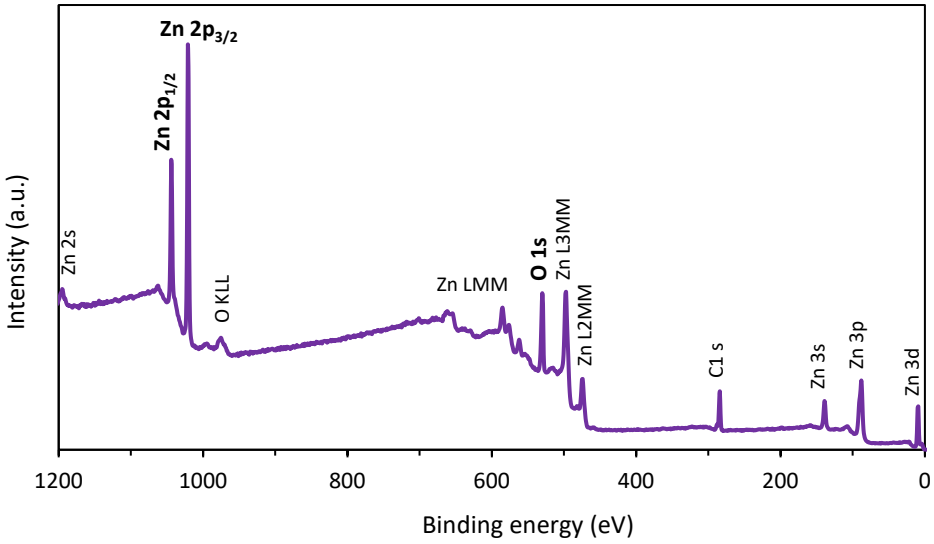

Figure 5. XPS wide survey spectra of the ZnO nanowires.

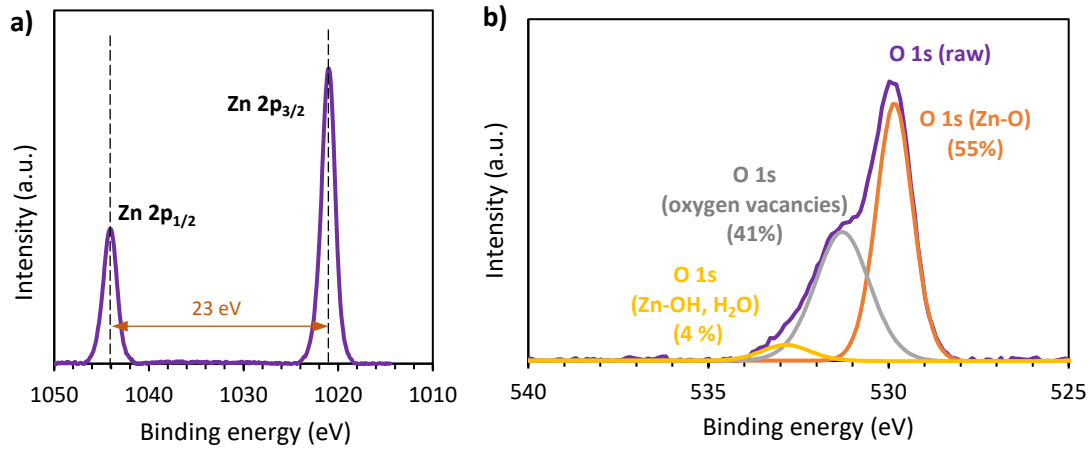

Figure 6. XPS spectra of Zn 2p (a) and O 1s (b) core levels of the ZnO nanowires.

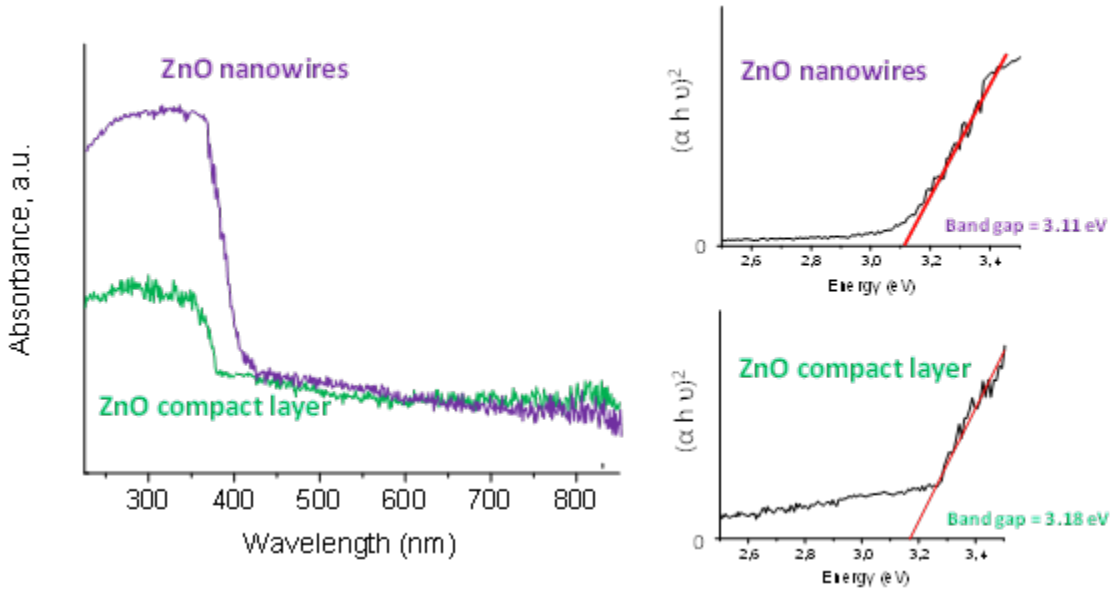

Figure 7. DR-UV-Vis. absorption spectra for ZnO samples with the determination of the bandgaps values.

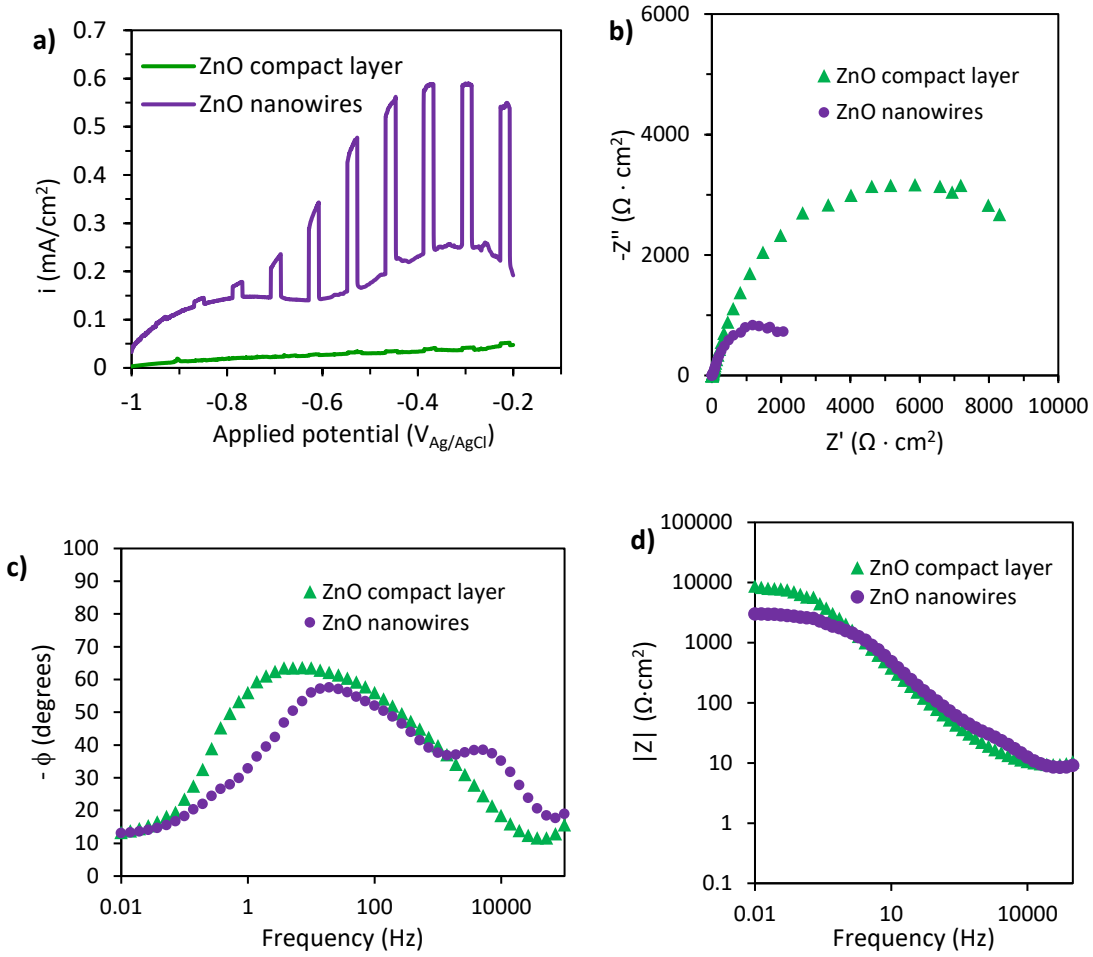

Figure 8. Current density versus applied potential in simulated sunlight on/off conditions (a). Nyquist (b), Bode-phase (c) and Bode-modulus (d) plots at an applied potential of -0.2 $V_{Ag/AgCl}$ under simulated sunlight conditions.

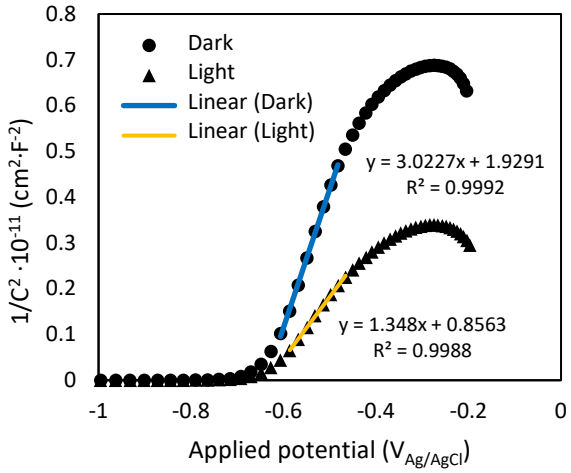

Figure 9. Mott-Schotkky plots in simulated sunlight and dark conditions.

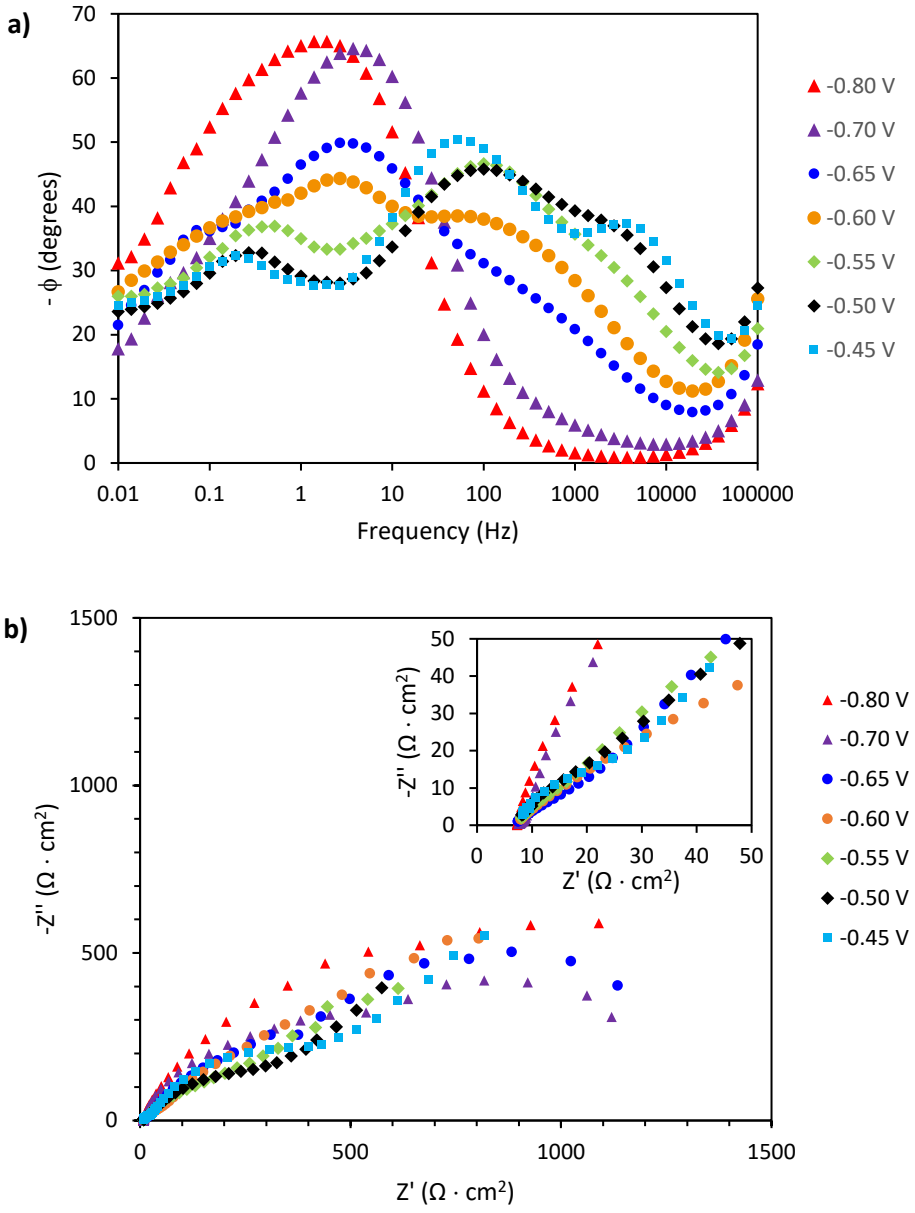

Figure 10. Bode-phase (a) and Nyquist (b) plots under illumination conditions at different applied potential ($V_{Ag/AgCl}$) near the flat band potential for the ZnO nanowires.

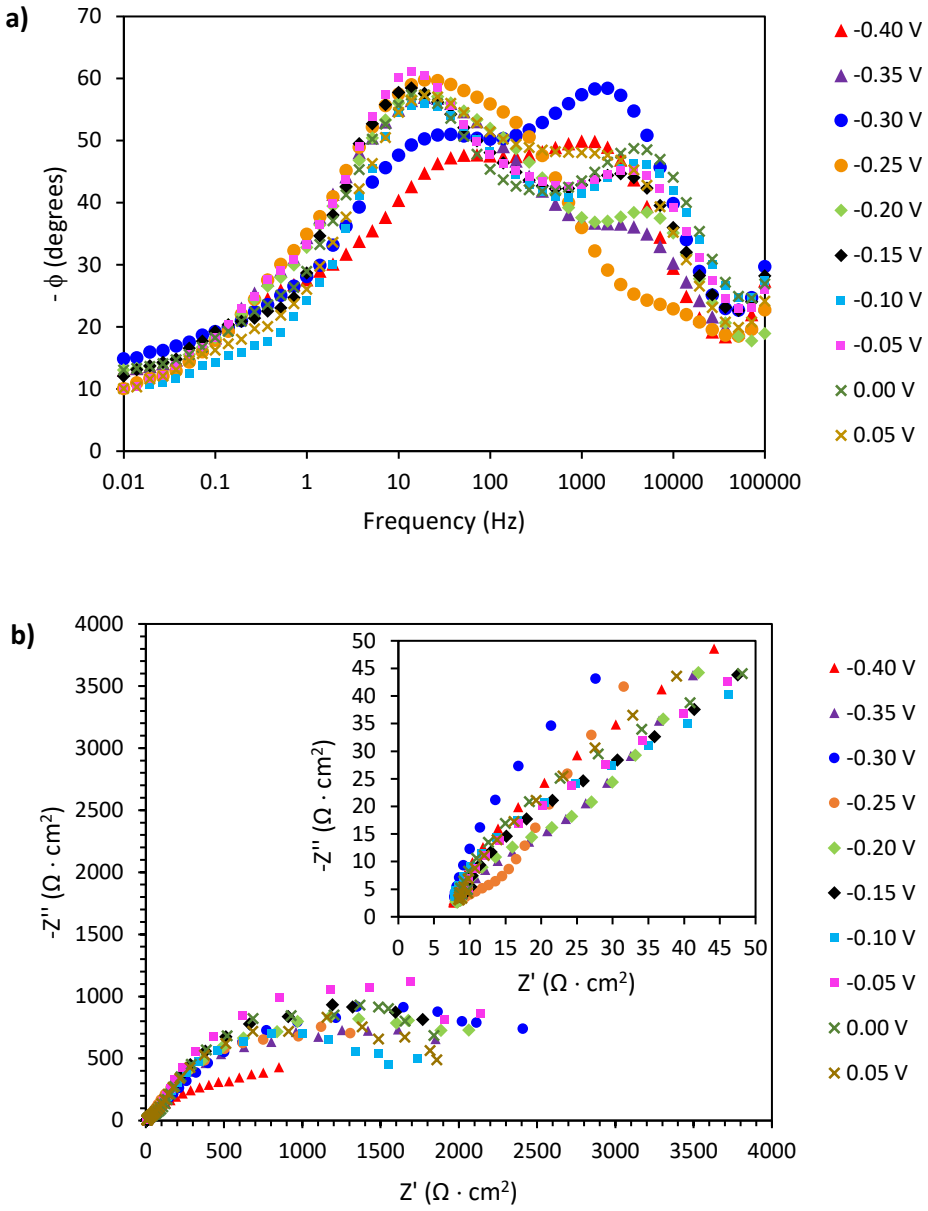

Figure 11. Bode-phase (a) and Nyquist (b) plots under illumination conditions at different applied potential ($V_{Ag/AgCl}$) beyond the flat band potential for the ZnO nanowires.

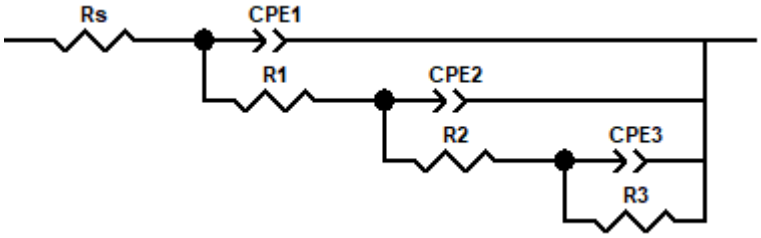

Figure 12. Equivalent circuit proposed for the description of the recombination and charge transfer processes in the ZnO nanowires.

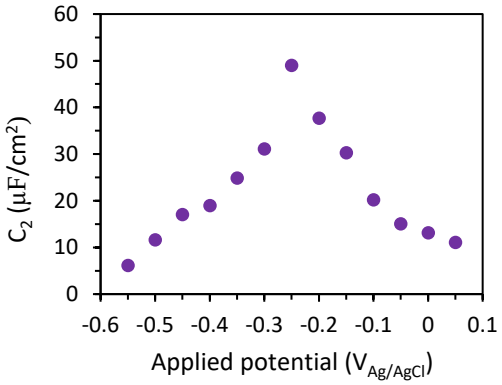

Figure 13. Charge transfer capacitance *vs.* applied potential beyond the flat band potential.